Wireless, battery-free, subdermally implantable platforms for transcranial and long-range optogenetics in freely moving animals

Jokubas Ausra[a], Mingzheng Wu[b,c], Xin Zhang[b,c], Abraham Vázquez-Guardado[d], Patrick Skelton[b,c], Roberto Peralta[e], Raudel Avila[f], Thomas Murickan[a], Chad R. Haney[g], Yonggang Huang[f], John A. Rogers[d,f,h,i,j,1], Yevgenia Kozorovitskiy[b,1], and Philipp Gutruf[a,k,l,m,1]

[a]Department of Biomedical Engineering, The University of Arizona, Tucson, AZ 85721; [b]Department of Neurobiology, Northwestern University, Evanston, IL 60201; [c]Chemistry of Life Processes Institute, Northwestern University, Evanston, IL 60208; [d]Simpson Querrey Institute, Center for Bio-Integrated Electronics, Northwestern University, Evanston, IL 60201; [e]Department of Aerospace and Mechanical Engineering, University of Arizona, Tucson, AZ 85721; [f]Department of Mechanical Engineering, Northwestern University, Evanston, IL 60208; [g]Center for Advanced Molecular Imaging, Radiology, and Biomedical Engineering, Northwestern University, Evanston, IL 60208; [h]Department of Materials Science and Engineering, Northwestern University, Evanston, IL 60208; [i]Department of Biomedical Engineering, Northwestern University, Evanston, IL 60208; [j]Department of Neurological Surgery, Northwestern University Feinberg School of Medicine, Chicago, IL 60611; [k]Department of Electrical and Computer Engineering, The University of Arizona, Tucson, AZ 85721; [l]Bio5 Institute, The University of Arizona, Tucson, AZ 85721; and [m]Neuroscience Graduate Interdisciplinary Program (GIDP), The University of Arizona, Tucson, AZ 85721

Edited by Kimani C. Toussaint, Brown University, Providence, RI, and accepted by Editorial Board Member Evelyn L. Hu June 16, 2021 (received for review December 15, 2020)

Wireless, battery-free, and fully subdermally implantable optogenetic tools are poised to transform neurobiological research in freely moving animals. Current-generation wireless devices are sufficiently small, thin, and light for subdermal implantation, offering some advantages over tethered methods for naturalistic behavior. Yet current devices using wireless power delivery require invasive stimulus delivery, penetrating the skull and disrupting the blood–brain barrier. This can cause tissue displacement, neuronal damage, and scarring. Power delivery constraints also sharply curtail operational arena size. Here, we implement highly miniaturized, capacitive power storage on the platform of wireless subdermal implants. With approaches to digitally manage power delivery to optoelectronic components, we enable two classes of applications: transcranial optogenetic activation millimeters into the brain (validated using motor cortex stimulation to induce turning behaviors) and wireless optogenetics in arenas of more than 1 m^2 in size. This methodology allows for previously impossible behavioral experiments leveraging the modern optogenetic toolkit.

transcranial | wireless | optogenetic | long-range | implantable

The recent emergence of wireless, battery-free, subdermally implantable optogenetic devices (1–5) dramatically expands experimental capabilities relative to tethered or external head-mounted methods. Critical advantages include minimized impact on behavior (6), device operation in multiple animals at the same time (1), and small form factor multimodal operation that combines optogenetic activation with, for example, fluid delivery (7). Collectively, these advances expand wireless optogenetic tools over tethered and battery powered technologies, broadening the scope of experimental paradigms that can be explored in small vertebrate models (3, 8).

Remaining fundamental limitations of wireless and battery-free systems relate to the nature of power delivery, which in most cases relies on magnetic resonant coupling (9) and mid-field (5) or far-field power delivery (10). All of these approaches suffer from power drop-offs as the device moves away from the power transmitting antenna (11). Existing power delivery solutions limit the use of these devices to ~13,500 cm^3 for continuous operation (3). Given this constraint, high-powered applications, such as optogenetic activation through the skull (12) or long-range operation in large spaces, cannot be achieved with the power harvesting capabilities of subdermally implanted devices. A realization of these capabilities would eliminate barriers in the design of experimental paradigms. This could enable diverse experiments that either leverage ethologically grounded, naturalistic environments that include burrows and obstacles for rodents (13) or those that take advantage of scale, for instance, allowing the exploration of neural mechanisms underlying the formation of hippocampal and entorhinal cortex "place" and "grid" cells in large environments (14, 15).

A separate potentially transformative benefit of the current advances involves increased delivered power for transcranial access. This application is optimal for longer wavelength-sensitive opsins due to superior tissue penetration by longer wavelength light (16). Transcranial activation of long wavelength-sensitive

Significance

Delivery of light for optogenetic stimulation of the brain is challenging, especially in small animals, because of behavioral constraints associated with physical tethering by fiber optic cables. This limitation interferes with some classes of in vivo behavioral experiments and makes others impossible. Additionally, the penetrating probes associated with these and related technologies cause damage to targeted regions of neural tissues, thereby complicating experimental evaluation. Here, we introduce a wireless, battery-free system that interfaces to the animal as a minimally invasive, subdermal implant capable of delivering high-intensity optogenetic light stimulation directly through the skull, without penetrating the brain. This approach avoids damage to brain tissue, facilitates simple surgical implantation, and enables new, ethologically grounded neuroscience experiments, applicable over large experimental arenas.

Author contributions: J.A., M.W., A.V.-G., P.S., Y.K., and P.G. designed research; J.A. performed electrical characterizations; M.W., X.Z., and P.S. performed behavioral experiments and immunohistochemistry; M.W. and X.Z. performed behavioral analysis; R.A. performed electromagnetic simulations; R.P. performed thermal and mechanical characterizations; A.V.-G. performed optical characterizations; Y.H. supervised finite element simulation; J.A. and T.M. fabricated devices; J.A., M.W., X.Z., A.V.-G., P.S., and C.R.H. analyzed data; and J.A., M.W., A.V.-G., P.S., R.P., R.A., J.A.R., Y.K., and P.G. wrote the paper.

The authors declare no competing interest.

This article is a PNAS Direct Submission. K.C.T. is a guest editor invited by the Editorial Board.

[1]To whom correspondence may be addressed. Email: jrogers@northwestern.edu, yevgenia.kozorovitskiy@northwestern.edu, or pgutruf@email.arizona.edu.

This article contains supporting information online at https://www.pnas.org/lookup/suppl/doi:10.1073/pnas.2025775118/-/DCSupplemental.

Published July 23, 2021.

opsins and halorhodopsins [e.g., ChrimsonR (590 nm) (17), ReaChR (590 nm) (18), C1V1 (590 nm) (19), Arch (566 nm) (20), NpHR (580 nm) (21), and ChRmine (635 nm) (22)] can eliminate the negative impact of penetrative probes on the brain (23), paving the way for less invasive in vivo neuroscience experiments especially relevant for studying reactive nonneuronal cell classes in the brain (24–26).

Here, we overcome the limitations described above by creating the means for harnessing energy continuously using highly miniaturized capacitive energy storage. Such capacitors have traditionally been used as buffer energy storage in passive devices (27–29). Here, we use the stored energy in conjunction with digital power management to deliver on-demand energy to optoelectronic components to provide high-energy light pulses and long-range operation. Specifically, this level of control enables transcranial optogenetic stimulation and long-range operation in arenas of large volume.

Results

Optogenetic activation is conventionally implemented by introducing light—typically using pulsed patterns—to neurons genetically modified to express light-gated opsin molecules (30). The energy requirement for a device that produces this stimulus is likewise pulsed, defining peak demand. When considering the average power demand, however, energy requirements are typically much lower because optogenetic activation usually operates with a duty cycle of at most 10 to 30% (31). To harness the energy between stimulation pulses, an energy storage is required that can retain the energy needed to buffer the delivery of one pulse of light while storing the energy harvested from the electromagnetic field without extensive losses. For subdermally implantable devices, several additional parameters have to be considered beyond storage capacity. The size, energy density, electrical characteristics, peripheral components needed for operation, and commercial availability are all important features to realize devices of broad utility to the neuroscience community. Based on these considerations, capacitive energy storage emerges as the most suitable technology because of the relatively high-energy density (1.38 J/cm^3 for a 0402 form factor 22 μF ceramic capacitor and 0.639 J/cm^3 for a 0201 2.2 μF ceramic capacitor, with an operational voltage limit of 5.6 V). Additionally, the capability to operate over a wide voltage range without the need for advanced management components, as well as rapid energy delivery, enables the support of high peak power demands. These ceramic capacitors are also available in small form factors that can be easily integrated into electronic circuits with schemes that enable system level flexibility critical to conform to curvilinear surfaces (32).

Fig. 1 shows one optogenetic activation cycle and the harvesting of energy in a wireless subdermally implantable device that employs capacitive energy storage. A three-dimensional (3D) rendering and photographic image of layered device construction is illustrated in Fig. 1*A*, highlighting the minimal footprint and profile that enable subdermal implantation. The capacitive energy storage of this device (1.38 J/cm^3) and total capacitive energy storage (2.76 mJ) is comprised of eight 22-μF (total of 176 μF) capacitors arranged in a parallel circuit. All components are commercially available and seamlessly integrate with the flexible circuit of the subdermally implantable device.

Key features of the operational scheme are highlighted in Fig. 1*B*, demonstrating the ability to supply currents of up to 2.6 A when discharged through a 0.5 Ω load. This, together with a low self-discharge rate (*SI Appendix*, Fig. S1), allows for flexible delivery of the power stored within the device. Fig. 1 *C*, *i* shows a simplified electrical circuit diagram of a capacitor bank enabled device. The capacitor bank stores up to 2.76 mJ of energy when fully charged with a voltage of 5.6 V. Fig. 1 *C*, *ii* illustrates the voltage over the capacitor bank in two use scenarios: a high load application, with high power pulse delivery to optoelectronic components for transcranial stimulation for short periods of time, and a low load application with regular optogenetic stimuli for extended periods of time. Both applications have similar average energy requirements of 0.11 mJ per pulse. Capacitors and the linear dropout regulator (LDO) can handle an unregulated voltage of up to 5.6 V and provide a stable output voltage (3.3 V for high load and 2.7 V for low load applications). The energy stored in the system, represented by the voltage that decays as energy is released, enables a utilization of a voltage drop from 5.6 to 3.3 V (Δ 2.3 V) for high load applications and from 5.6 to 2.7 V (Δ 2.9 V) for low load applications. This operational voltage range results in 2.1 mJ of usable energy in the capacitor bank for low load applications and 1.8 mJ for high load applications.

Illumination events of the micro-inorganic light-emitting diode (μ-ILED) load are highlighted in Fig. 1 *C*, *ii*. Here, the two rates of current delivery sourced from the capacitor bank are shown. For high currents, the corresponding voltage at the capacitor bank decays rapidly and can provide high intensities of light for a short pulse. If the current demand is reduced, longer stimuli are enabled at the same energy harvesting rate. Following from these operational parameters, two discrete modes for use in optogenetics are demonstrated in this work, transcranial stimulation and long-range applications in enlarged arenas. While we focus on optogenetic stimulation applications, the current advance can benefit various battery-free device categories, such as photometry methods (6), electrical stimulation for heart defibrillation (2) or deep brain stimulation (33), and controlled drug delivery schemes (34).

Expanding Arena Volume for Optogenetics. Harnessing the capabilities of the capacitive storage significantly expands arena sizes for wireless battery-free optogenetics. Fig. 2 explores the electrical, mechanical, and optical design characteristics of devices tailored to work in large arena volumes (3). Scenarios combining a range of duty cycles and intensities at specific input powers are graphically represented in Fig. 2*A*. In a typical use scenario, device duty cycles and irradiances of 20% and 10 mW/mm^2, or duty cycles and irradiances of 10% and 25 mW/mm^2, represent frequently chosen parameters (31). These can be guaranteed to operate with as low as 0.75 mW electrical power continuously supplied to the implant.

The energy supplied by the capacitor bank is harnessed by an LDO (2.7 V) to stabilize the operational voltage and a small outline microcontroller (μC) that controls the μ-ILED in current sink configuration, shown in an electrical schematic in Fig. 2*B*. Component selection is made with miniaturization as a priority, with details presented in *Materials and Methods*. The result is an 87-mg device with dimensions of 13.50 × 10.26 × 0.89 mm and displacement volume of 20.4 mm^3.

A layered rendering of the device capable of long-range operation in freely moving subjects is displayed in Fig. 2*C*. The capacitor bank for energy storage is located beneath the bottom copper layer to reduce the electronics footprint, enabling flexible placement of the injectable light source within the device perimeter. Magnetic resonant coupling (13.56 MHz) between the primary antenna surrounding the experimental arena and the secondary millimeter-scale antenna on the device provides energy wirelessly. Encapsulation is realized with a layer of parylene to create a thin, flexible platform capable of seamless mechanical integration with the curved skull. Commercial availability of the components allows for high reproducibility and enables scalable fabrication.

A photographic image of the device in Fig. 2*D* highlights the thin and flexible form factor that facilitates subdermal implantation in rodents. The serpentine structure connecting the main body with the probe is designed to stretch extensively during the surgical procedure. The photographic image in Fig. 2*E* demonstrates this capability, and the *Inset* displays the result of a finite

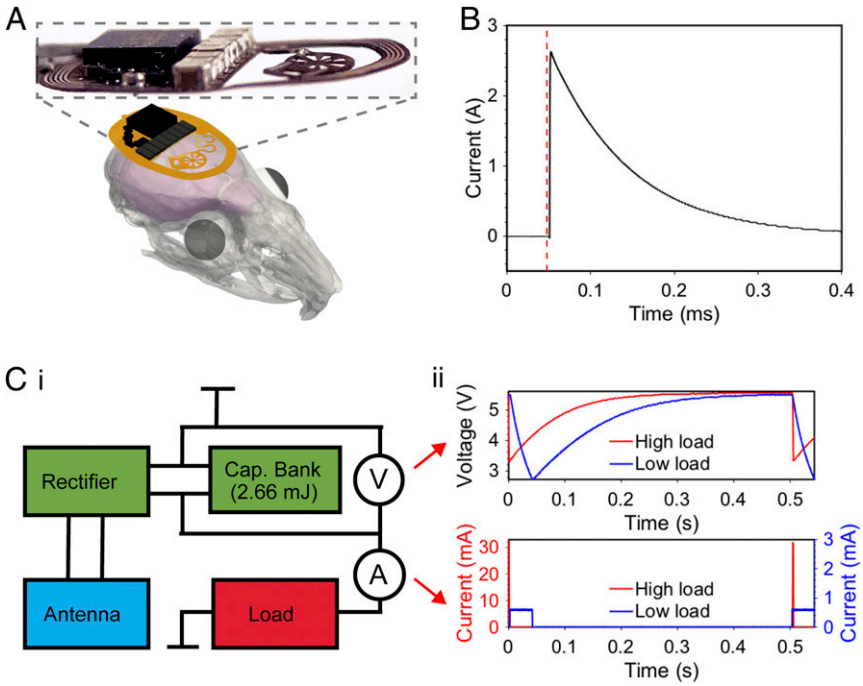

Fig. 1. Overview and key operational characteristics of a wireless, subdermally implantable device with capacitive energy storage. (*A*) 3D rendering and photographic image of device highlighting the minituarized profile. (*B*) Operational schematic showing current output from capacitive energy storage. (*C, i*) Simplified device circuit diagram (*ii*) with voltage measurements of capacitor bank and current measurements of load for high load and low load applications.

element simulation, described in detail in *Materials and Methods* and *SI Appendix*, Fig. S2, subjecting the serpentine to 110% strain (5.53 mm displacement). Here, the copper layer experiences a maximum strain of 3.58% within the elastic regime, enabling repeated strain cycles of the serpentine without loss in conductivity (2). This robust strain performance allows for a facile placement of the probe within the perimeter of the device to target various brain regions as well as the periphery. Strain performance is also key for enabling normal animal movement without device breakdown.

Primary antenna performance is critical for operation in large experimental arenas. To cover large volumes and surface areas, the primary antenna is configured in a dual loop arrangement (4- and 11-cm loop from cage floor) over an arena of 70 × 70 cm. Fig. 2*F* showcases a finite element simulation of the magnetic field; details of the simulation are described in *Materials and Methods*. The resulting magnetic field strength is symmetric throughout the cage with a slight reduction near the tuner and loop crossover, with elevated magnetic field density in the corners. This reflects comparable field distribution to smaller enclosures (2). The key insight of the simulation, however, is that larger antennas become difficult to properly tune at 13.56 MHz operational frequency because the self-resonance approaches the working frequency of the system (*SI Appendix*, Table S1) and effectively limits cage sizes to 70 × 70 cm with a dual loop antenna setup.

Power harvesting of the secondary antenna, the antenna on the implant, is maximized by optimizing the number of turns in the coil. The power harvesting behavior of devices with equivalent trace spacing (100-μm wide traces with 50-μm spacing) with six, eight, and 10 turns are compared by incrementally increasing the device load shown in Fig. 2*G*. The harvesting capabilities of 1.34 mW are obtained with a 10-turn device at a voltage of 3.67 V and a load of 10 kΩ in the center of a 70 × 70-cm arena at a height of 3 cm from the arena floor (10 W radio frequency [RF] input power). These parameters match the device's operating voltage during capacitor bank recharge events. The corresponding measurements of power distribution throughout the large cage with a 10-turn device and an RF input of 10 W is shown in Fig. 2*H* at physiologically relevant heights of 3, 6, and 8 cm (additional details in *SI Appendix*, Fig. S3 *A–C*). Antenna performance is optimized for large enclosures. Performance in smaller arenas is characterized in *SI Appendix*, Fig. S3*D*. Following this optimization, sufficient energy to operate devices at the duty cycle and intensity combinations highlighted in Fig. 2*A* is available at the implant, enabling experimental paradigms that utilize the whole volume of the experimental arena. Operational area and volume are 4,900 cm^2 and 68,600 cm^3, respectively, reflecting a 444% increase in surface area and 408% increase in volume over prior work (1, 3, 4). The enclosed volume can be flexibly arranged. For example, an increase in vertical space (68,600 cm^3) for use with flying species is shown in *SI Appendix*, Fig. S4*A*, demonstrating power levels comparable to other arenas for two-dimensional moving species in this work (*SI Appendix*, Fig. S4*B*). Device operation in even larger arenas (9,400 cm^2) can be achieved by combining multiple antennas and RF power sources. In a proof of principle experiment, we demonstrate outfitting the floor of an experimental arena with two single loop antennas (65 × 65 cm) with 15-cm spacing to result in a coverage of 145 × 65 cm. The distance between the antennas is chosen to be sufficiently far to minimize resonant interaction but close enough for the near field to extend outside the primary antenna loop. This design allows powering devices located between the antennas (*SI Appendix*, Fig. S5). Minimum power in this experimental arena is 0.59 mW, enabling the operation of standard (invasive) optogenetic activation protocols in previously unattainable arena sizes for untethered animals.

The capability to supply a range of system voltages enables the utilization of various μ-ILEDs that feature turn-on voltages of 1.8 to 2.6 V. Thus, these systems can control a variety of opsins (17–20, 35) and halorhodopsins (21). A photographic image of multiple devices powered simultaneously, with a range of activation wavelengths operating in a 70 × 70-cm enclosure, is shown in Fig. 2*I*. Current–voltage (I–V) curves for blue, red, and orange μ-ILEDs

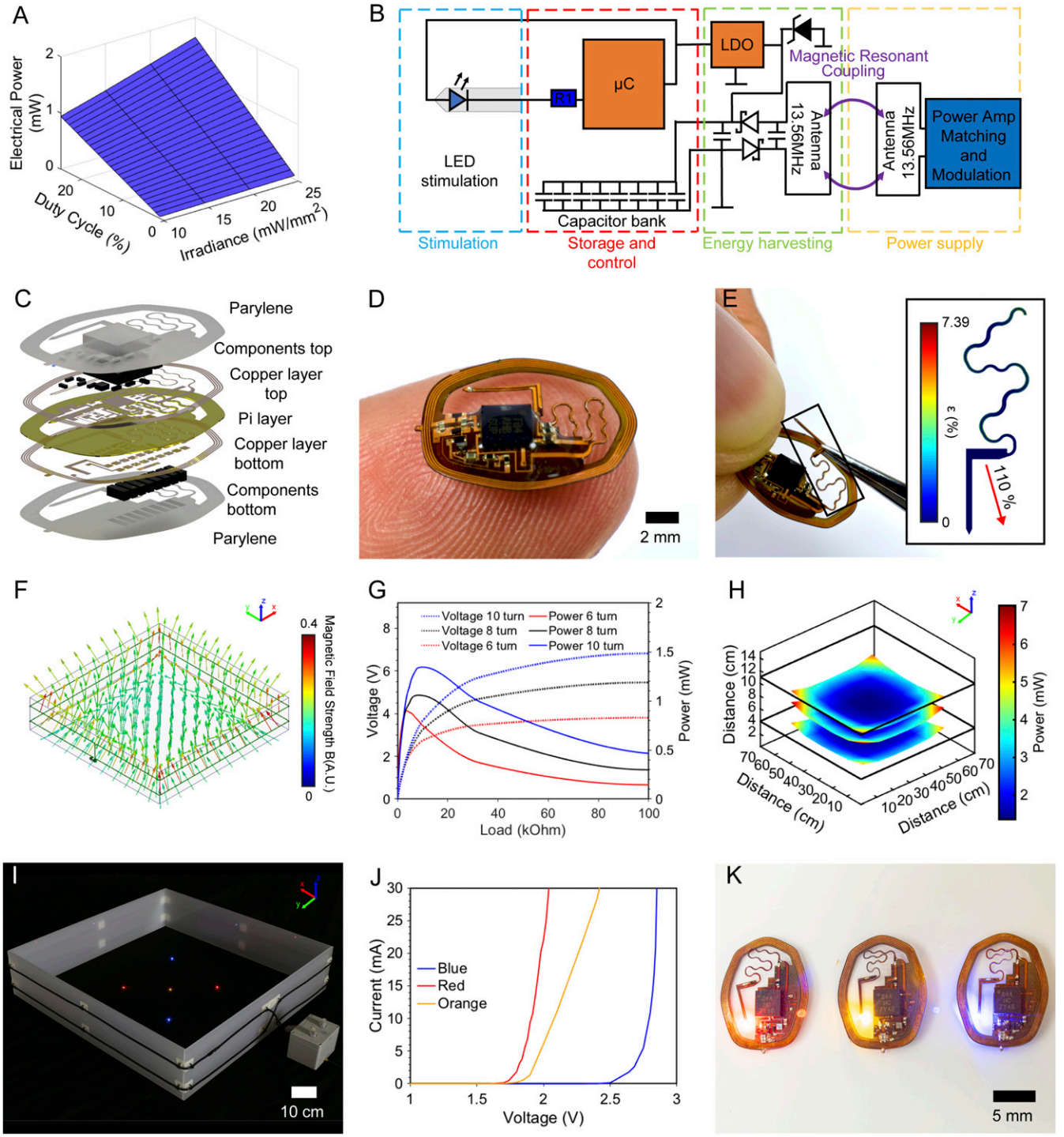

Fig. 2. Operation principle and electrical, mechanical, and optical characterization of the long-range device. (*A*) Average electrical power consumption for a range of duty cycles and irradiances. (*B*) Electrical operation principle schematic. (*C*) Layered rendering of device structure. (*D*) Photographic image of device balanced on a finger. (*E*) Photographic image of device serpentine being stretched. (*Inset*) Mechanical strain finite element simulation. (*F*) Magnetic finite element simulation for a 70 × 70-cm arena. (*G*) Rectification behavior of a long-range device with 6, 8, and 10 turns in the center of a 70 × 70-cm arena at a height of 3 cm and an input power of 10 W. (*H*) Power distribution of 10-turn device in a 70 × 70-cm arena with 10 W input power at heights of 3, 6, and 8 cm from the arena floor. (*I*) Photographic image of devices with red, orange, and blue μ-ILEDs activated in a 70 × 70-cm arena. (*J*) IV curves for red, orange, and blue μ-ILEDs. (*K*) Photographic image of devices with red, orange, and blue μ-ILEDs.

and corresponding images of devices equipped with the optoelectronic components are shown in Fig. 2 *J* and *K*, respectively.

In Vivo Characterization of Implanted Devices. Device operation is verified visually in a typical open field experimental arena (50 × 50 × 40 cm) for mice. Fig. 3*A* shows a photographic image with a subject during an open field behavioral assay with active optogenetic stimulation (dual loop antenna, 8 W RF input). Device performance is consistent throughout the assay and is documented in Movie S1, showing a freely moving subject during

active stimulation with a probe subdermally implanted facing toward the epidermis for visual confirmation of device function. An additional advantage of utilizing ceramic capacitors as an energy storage for devices is the minimal impact on 3D imaging, enabling the use of MRI and computed tomography (CT). This overcomes imaging challenges for devices that contain magnetic components (7). The combined 3D rendering of an MRI and CT image is shown in Fig. 3*B*. The side view shown in Fig. 3*C* highlights the small footprint, thin makeup, and soft mechanics of the device that enable facile subdermal implantation on the skull and ensure fast recovery.

To evaluate whether locomotor behavior is altered by the presence of a subdermally implanted device, in the absence of stimulation or opsin expression, we measured the distance traveled in an open field arena for several mice. Example trajectory maps for a control animal and an animal with an implant are shown in Fig. 3 *D* and *E*, respectively. The total distance traveled and exploration rates did not vary between mice with and without an inactive implant (Fig. 3*F*), suggesting that the subdermal implant has a minimal impact on basic aspects of locomotion, unlike external cables used in wired optogenetics (36).

Transcranial Optogenetic Stimulation. Transcranial stimulation has previously been realized in anesthetized animals with high-intensity light pulses that penetrate the skull without invasive procedures (12). Due to technological limitations—low current delivery capabilities, low voltage, and the relatively large form of currently available miniaturized batteries—this approach has not been demonstrated in freely moving subjects with a wireless configuration. Here, we introduce a device specifically optimized for transcranial optogenetic stimulation in freely moving subjects.

Fig. 4*A* outlines the operational parameter space for this class of devices. In this stimulation regime, very high light intensities can penetrate the skull and reach areas of interest in the brain while keeping the blood–brain barrier intact (*SI Appendix*, Fig. S6). An example of typical parameter choices to enable transcranial stimulation is a duty cycle of 1% (10 Hz, 1-ms pulses) and a high optical power of 13 mW that can be sustained with electrical power harvesting of 0.71 mW. Here, optical power demands are balanced by a lowered duty cycle well within the commonly used parameters (37), enabling high-energy events even when wireless power harvesting is relatively low. Wireless programming of stimulation parameters (*SI Appendix*, Figs. S7 and S8 *A–C* and Movie S2) is enabled by a custom ON/OFF keying protocol modulated using the transistor–transistor logic (TTL) control of a commercially available RF amplifier (Neurolux, Inc.). Low latency startup of stimulation upon application of the RF field (*SI Appendix*, Fig. S8*D*) makes the control of optical pulse trains for this class of devices comparable to other wireless and battery-free implants.

The electrical configuration shown in Fig. 4*B* highlights key components and antenna designs that enable the delivery of high-intensity light pulses while reducing device weight to 76 mg, with dimensions of 11.73 × 7.95 × 0.39 mm. Specifically, the current-limiting resistor, which determines light intensity, is substantially reduced (1 ± 0.05 Ω) to enable currents up to 30 mA, limited by the internal resistance of the μC (30 Ω) in current sink configuration. Furthermore, LDO voltage (3.3 V) is chosen to enable increased current delivery for the red μ-ILEDs (2.2 V at 30 mA) to produce high-powered pulses for transcranial optogenetic stimulus.

Fig. 4*C* shows an exploded view schematic of the transcranial device. The positioning of the capacitor bank to the front of the device, to enable a flush mounting of the system with the skull, is critical for the implantation process. A photographic image of the device balanced on a finger is shown in Fig. 4*D*, highlighting the miniaturized form factor resulting in a device volume of 17.9 mm^3. The star-shaped μ-ILED holder has been engineered to enable facile surgical application to the skull. The tab, reinforced with copper strips that plastically deform, keeps the shape when bent to a 90° angle prior to the surgery for mounting in a

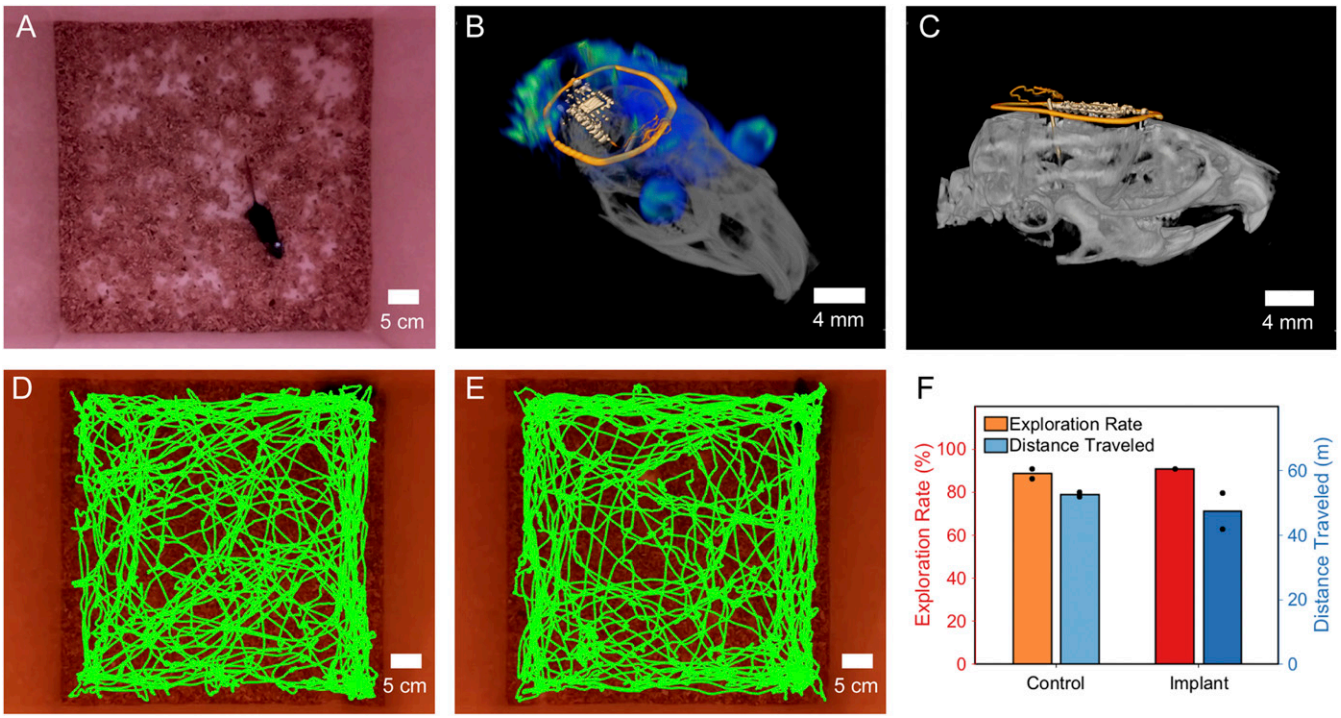

Fig. 3. 3D imaging and impact on behavior. (*A*) Device operation in a mouse in a 50 × 50-cm cage with 8 W RF input. (*B*) Combined MRI and CT 3D rendering of a device implanted in a mouse. (*C*) Side view CT of the implanted device. (*D*) Trajectory map for a control animal. (*E*) Trajectory map for animal with device implanted. (*F*) Comparison of exploration rate and distance traveled for control animal and animal implanted with device.

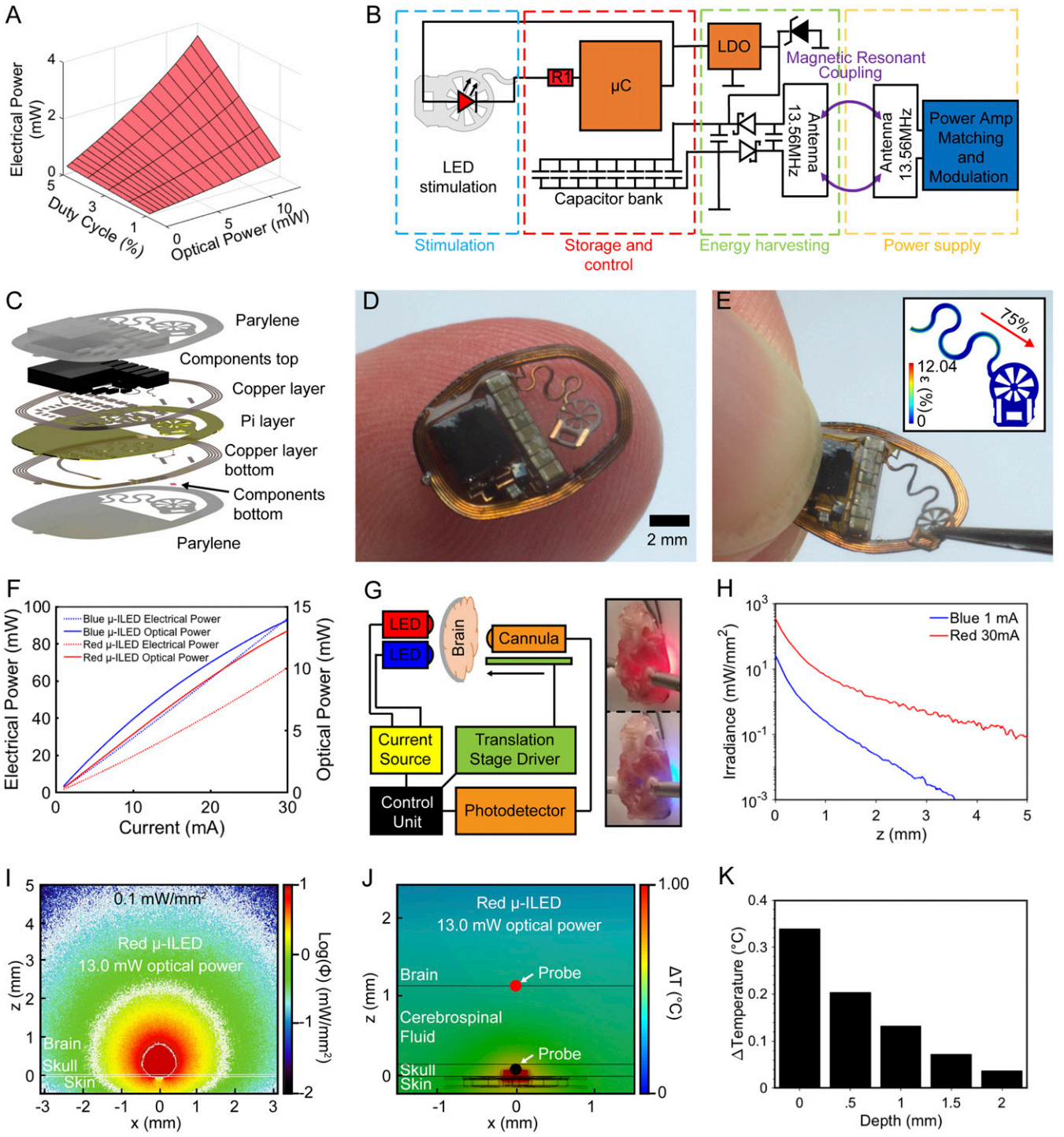

Fig. 4. Transcranial device operation principles and characterization. (*A*) Average power required for combinations of duty cycles and optical powers. (*B*) Electrical schematic of the device for high-intensity stimulation. (*C*) Rendering of device layer structure. (*D*) Photographic image of a device balanced on finger. (*E*) Photographic image of a strained device. (*Inset*) Finite element simulation indicating applied and resulting strain. (*F*) Electrical and optical power with increasing current for blue and red μ-ILEDs. (*G*) Schematic of the setup used for line measurements of blue and red light irradiance through skull and brain. (*H*) Irradiance measurements for mouse skull and brain for red and blue μ-ILEDs. (*I*) Monte Carlo simulation of light propagation through skull for a red light source with 13-mW optical power. (*J*) Thermal impact analysis of red μ-ILED with 13-mW optical power at steady state. (*K*) Experimentally measured brain temperature for an intact skull at increasing brain depth from site of μ-ILED with transcranial stimulation device operated at 10 Hz and 1% duty cycle for 5 min.

stereotactic setup. The star-shaped flexible substrate further enables precise alignment of the device with the target because of increased visibility of markers on the skull, and it offers a large surface area for surgical adhesives. Surgical procedures are outlined in detail in *Materials and Methods* and in *SI Appendix*, Fig. S9.

To enable flexible placement within the device perimeter, serpentine interconnects are engineered to accommodate movement

as shown in the photographic image of Fig. 4*E*. The *Inset* displays a finite element simulation with 75% strain applied (2.05-mm displacement), which results in a strain of 3.61% in the copper layer. This strain level is below plastic deformation, enabling repeated placement of the probe without impact on performance. Details on the finite element simulation can be found in *SI Appendix*, Fig. S10.

Optical output power of the device for two different μ-ILED wavelengths is characterized in Fig. 4*F*. Electrical power input and the resulting optical power is measured using an integration sphere as detailed in *Materials and Methods*. The μ-ILED can provide a maximum optical power of 14 and 13 mW for blue and red μ-ILEDs, respectively, with a maximum current of 30 mA, resulting in a power consumption of 92 and 67 mW, respectively. This results in an efficiency of 19.4% for red and 11.4% for blue μ-ILEDs at 30 mA. The increased efficiency and longer wavelength of red light, which is less prone to absorption by tissue and bones, makes red light appropriate for transcranial stimulation of deep brain regions.

A customized apparatus is used to measure light propagation in the intact skull and brain of mice (Fig. 4*G*). The optical power measured along the normal plane from the μ-ILEDs for different input optical powers is plotted in Fig. 4*H* for both red and blue μ-ILEDs. These results show that 13.05 mW of optical power (226.56 mW/mm^2 irradiance at the μ-ILED's surface) penetrates 5 mm through the skull and brain with an irradiance three order of magnitude lower (0.22 mW/mm^2) for red light μ-ILEDs. This result is above the illumination threshold for red-shifted opsins (17).

These experimental results form the basis for a Monte Carlo simulation to predict penetration of red light through the skull. A multilayer domain is implemented to consider a skull thinned to 50 μm, the skin over the skull, and the brain tissue. The photon fluence, equivalent to the irradiance of illumination, normalized with respect to the input optical power for the red (13.05 mW, Fig. 4*I*) and blue μ-ILEDs (0.88 mW, *SI Appendix*, Fig. S11) predicts illumination volume on the order of 87.07 and 1.54 mm^3, respectively. In addition, the transcranial propagation depth into the brain tissue, at a reference irradiance threshold of 0.1 mW/mm^2, is expected to reach 4.8 mm for red and 1.4 mm for blue illumination (*SI Appendix*, Fig. S11).

There is a direct correlation of light propagation estimated using Monte Carlo simulation and obtained experimentally for both red and blue μ-ILEDs. The predictions made using Monte Carlo simulations with subsequent experimental validation yield a powerful strategy to predict outcomes of illumination, especially in the context of parameters provided by the transcranial devices described here. These illumination parameters are appealing for numerous scenarios of optogenetic neuronal manipulation, especially for the activation of larger areas and deeper subcortical regions of the brain.

Steady-state finite element simulations in Fig. 4*J* show the thermal impact of high-intensity pulses on physiology. The thermal impact of the light source is simulated with a 54.1-mW thermal power input, a value derived from the previously measured electrical input power and efficiency of the μ-ILED, which is represented by a 0.24 × 0.24 × 0.1-mm thermal actuator site. The thermal power is representative of the maximum operational conditions the wireless and battery-free electrical system is capable of, which is created by 13-mW optical input power at the μ-ILED location with 10 Hz frequency and 1% duty cycle. Here, a starting temperature of 36 °C is selected without considering perfusion of the tissue, resulting in a worst-case estimate, as temperatures in vivo are expected to be lower due to cerebrospinal fluid (CSF) perfusion. Details can be found in *Materials and Methods* and in *SI Appendix*, Fig. S12. From the simulation, it is evident that heat preferentially spreads toward the skin of the scalp, which has a relatively high thermal conductivity of 0.56 $W \cdot m^{-1} \cdot K^{-1}$, and only a fraction of the heat penetrates the skull and enters the CSF and brain surface. Thermal impact on the skull in this condition never exceeds 0.90 °C, and thermal impact on brain tissue never exceeds 0.37 °C. Experimental measurements of the thermal impact are validated by using an intact mouse skull ex vivo with a device external to the skull. The results indicate a strong match to predicted temperature from finite element modeling as shown in Fig. 4*K* and *SI Appendix*, Fig. S13.

Finite element simulations for a thicker skull (0.25 mm, representing a skull without surgical alteration) show a steady-state temperature of 0.25 °C at the CSF/brain interface, a 32% reduction in thermal impact compared to a thinned skull (*SI Appendix*, Fig. S14). Optical penetration depth is not significantly affected for red-shifted opsins by maintaining a thicker skull (*SI Appendix*, Figs. S15 and S16). Here, illumination volume in comparison to a thinned skull is reduced by ∼20% for red light and 60% for blue light. Transient simulations performed in the thinned skull model at two indicated probes located at the skull/LED and brain/CSF interfaces are used to record the transient temperature change over a 5-s period for a μ-ILED operating at 10 Hz and 1% duty cycle. The results of these investigations are shown in *SI Appendix*, Fig. S17 and Movie S3). Here, a short-term temperature increase of 2.55 °C occurs at the skull/LED interface with an average increase of 0.247 °C after 5 s. Temperatures at the brain/CSF interface show no pulsatile component. Because of the low increases in temperature in the worst-case scenario that does not include perfusion cooling, we do not expect substantial thermally driven changes in neuronal activity (38).

Transcranial Optogenetic Stimulation of Secondary Motor Cortex in Freely Moving Mice. To demonstrate the feasibility of transcranial stimulation using wireless optogenetic devices with capacitive power storage in freely behaving mice, we target the secondary motor cortex (M2) that produces robust motor behavior upon activation (39). A CT image of the subdermally implanted device is shown in Fig. 5*A*. Adult mice are injected with an adeno-associated virus encoding the red light–sensitive channelrhodopsin ChrimsonR [AAV9-syn-ChrimsonR-tdT (17)] or EGFP (AAV8-syn-EGFP) in the right M2 (Fig. 5 *B* and *C*). Devices are implanted 2 to 3 wk later following a standard procedure, with optional skull thinning over the site of injection to maximize light penetration (40). Animals are allowed to recover for at least 2 d before behavioral experiments. The devices are programmed to provide tonic high frequency stimulation at 20 Hz (2 ms pulse width, 628 nm). Our data demonstrate that unilateral wireless transcranial optogenetic stimulation in M2 produces robust rotational behaviors in mice expressing ChrimsonR (representative video sequences in Movies S4 and S5), while mice expressing fluorophore control do not show significant rotational behavior during stimulation (Fig. 5 *D*–*H*). These results confirm that the devices substantially activate opsins in cortical regions through the skull. The activation is unlikely to be caused by nonspecific thermal effects since mice without opsin expression do not display significant behavioral changes. To further confirm the activation of motor neurons, a subgroup of mice expressing ChrimsonR received light stimulation before tissue harvesting to induce neuronal activity-driving immediate early gene expression (c-Fos). The number of c-Fos–positive cells and individual c-Fos intensities are significantly higher in the M2 of mice that received stimulation comparing to no-stimulation controls (Fig. 5 *I* and *J*). Altogether, our results demonstrate clear optogenetic effects on motor behavior and neuronal activity, supporting the capability of high-intensity operation of the presented wireless platform to achieve transcranial activation.

Discussion

The wireless battery-free and fully implantable optogenetic activation devices presented here utilize miniaturized, digitally managed capacitive energy storage to harvest otherwise lost energy.

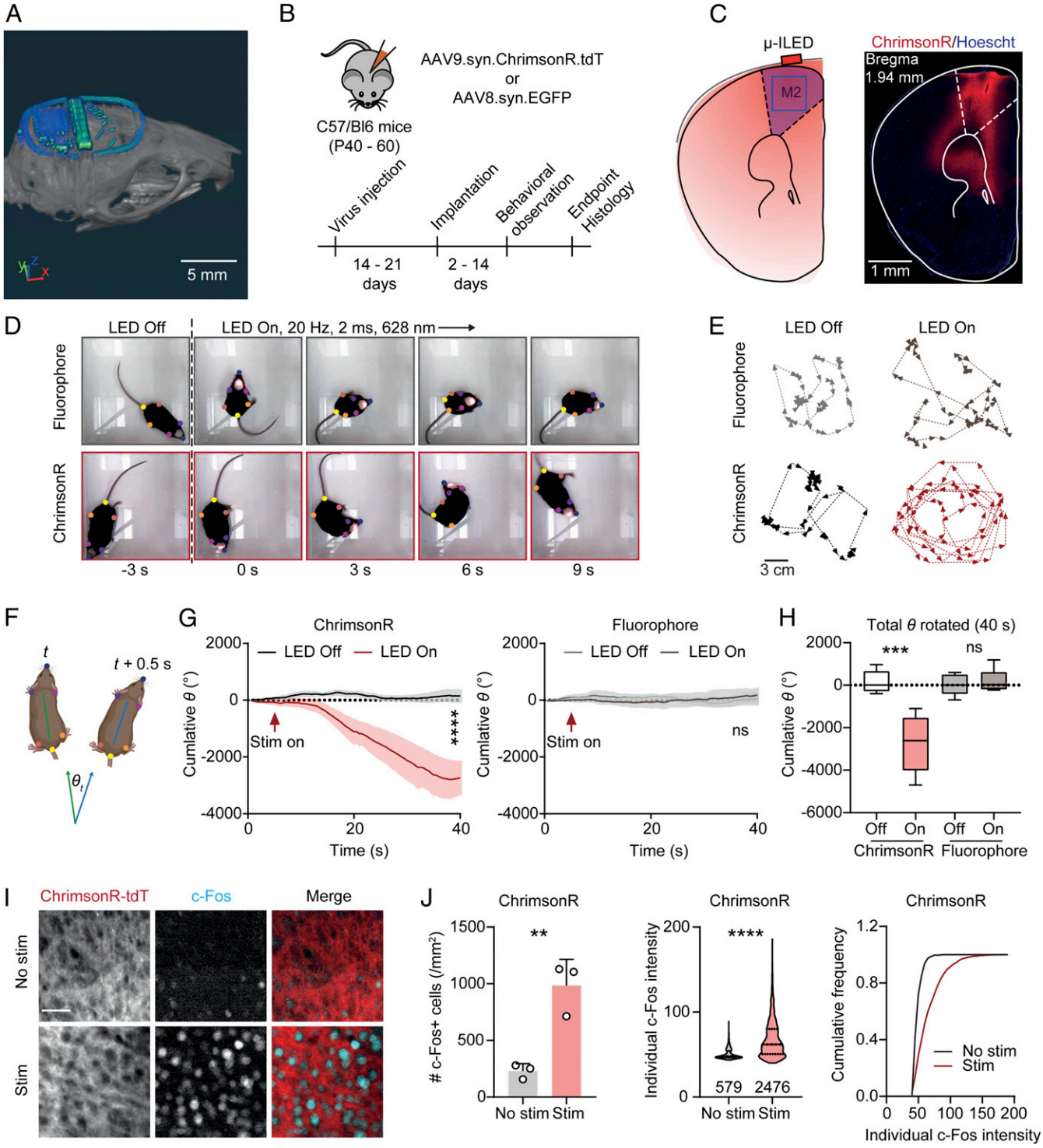

Fig. 5. Transcranial optogenetic stimulation in M2 drives rotational behavior. (*A*) CT image of a subdermally implanted device on the skull of a mouse (Scale bar: 5 mm). (*B*) Schematic of virus transduction and experimental timeline. (*C*) Schematic of transcranial optogenetic stimulation in M2 and an example image of ChrimsonR expression (Scale bar: 1 mm). (*D*) Example frames across a 9-s long stimulation episode. Colored dots show the body positions tracked using Deeplabcut. (*E*) Example traces of mice expressing fluorophore or ChrimsonR with or without transcranial optogenetic stimulation (Scale bar: 3 mm). (*F*) Schematic illustrating the calculation of rotation degree (θ) for each frame (0.5-s bin). (*G*, *Left*) Summary data showing the cumulative rotation degrees in mice expressing ChrimsonR during a 40-s long episode. Two-way ANOVA, LED Off versus LED On (column effect), $P < 0.0001$. (*Right*) Same as *Left* but for mice expressing control fluorophore. Two-way ANOVA, LED Off versus LED On (column effect), $P = 0.2074$. $n = 5$ mice/group. (*H*) Summary data showing the total degrees rotated in each experimental condition. One-way ANOVA, $F(3, 16) = 14.90$, $P < 0.0001$, Sidak's multiple comparisons, LED Off versus On: ChrimsonR, $P < 0.0001$, fluorophore, $P = 0.9621$. $n = 5$ mice/group. (*I*) Example images of c-Fos staining in M2 of mice expressing ChrimsonR-tdT with or without transcranial optogenetic stimulation (Scale bar: 50 μm). (*J*) Summary data showing the number of c-Fos neurons in individual mice (*Left*), the distribution of individual c-Fos particle intensities (*Middle*), and cumulative frequency of c-Fos particle intensities (*Right*). Two-tailed unpaired Student's *t* test, No stim versus Stim: no. c-Fos+ cells, $P = 0058$; individual c-Fos intensity, $P < 0.0001$. $n = 3$ mice/group. Data represent mean ± SEM; the lines in the box and violin plot show quartiles and median. $^{**}P < 0.01$, $^{***}P < 0.001$, $^{****}P < 0.0001$.

This allows us to power events that exceed harvesting capabilities of conventional optogenetic stimulation devices to enable two applications—operation in large arenas and transcranial optogenetic stimulation. This approach more than quadruples usable arena volumes from 13,500 to 68,600 cm^3 (3) with a single antenna design, and it can be scaled to very large arenas with multiple antenna and RF supplies. The capability to deliver energy in high-powered pulses increases the light output capability of wireless, battery-free devices by 1,175% over previous reports, enabling wireless transcranial stimulation previously only achieved in head-fixed and anesthetized animals. Ex vivo measurements and Monte Carlo simulations reveal sufficient penetration in deep brain regions to activate widely available red-shifted opsins (27). We demonstrate that high-powered light pulses from the wireless, battery-free subdermal implanted devices can transcranially stimulate the motor cortex to evoke motor responses.

Collectively, these devices significantly expand experimental paradigms for neural activity control in freely moving subjects in ethologically relevant environments and with minimally invasive transcranial optogenetics. Fundamentally, the strategies introduced and demonstrated here for small rodent subjects also apply to other animal models, including 3D navigating species and larger animals. The expansion of the 3D environment size optimizes experiments for 3D mobile birds and bats (41–43), also opening the door for innovative experiments in primates, which leverage the recent developments in genetic traction for these models (44, 45). Transcranial optogenetic stimulation enabled by the high-intensity operation mode substantially reduces the physical damage to the connectivity of the targeted brain regions. Notably, this transcranial light delivery method provides a unique alternative for the optogenetic studies that involve reactive non-neuronal cells (e.g., glia and immune cells), eliminating gliosis and the immune system response caused by intracranial implants (46–48). Finally, energy delivery and management strategies may provide the foundation to advance fidelity of other techniques that have recently been shown in wireless and battery-free device formats, including photometry and phototherapy as well as electrical stimulation for cardiac and neural systems.

Materials and Methods

Device Fabrication. Pyralux AP8535R served as the substrate for the flex circuit. Direct laser ablation (LPKF U4) was used to structure the top and bottom copper layers (17.5 μm) on the substrate polyimide layer (75 μm). Ultrasonic cleaning (Vevor; Commercial Ultrasonic Cleaner) was carried out with flux (Superior Flux and Manufacturing Company; Superior no. 71, 10 min) followed by an isopropyl alcohol (MG Chemicals, 2 min) wash. The devices were rinsed with deionized (DI) water to remove any remaining particles. Copper wire (100 μm) and low-temperature solder (Chip Quik; TS391LT) were used for via connections. After assembly, device components were fixed in place with ultraviolet (UV)-curable glue (Damn Good 20910DGFL) followed by curing with a UV lamp (24 W) for 5 min. The devices were encapsulated with parylene coating via chemical vapor deposition.

Electronic Components. The careful selection of electrical components enabled a minimal device footprint, outline, and volume. Low-temperature solder (Chip Quik; TS391LT) was used for the manual soldering of components onto the device. A rectifier composed of two Shottky diodes (40 V, 30 mA, MCC RB751S-40DP) and a tuning capacitor of 82 pF (TDK, CGA2B3 × 7R1H104K050BE) and a 2.2-μF smoothing capacitor (Samsung CL03A225MQ3CRNC) were used for the rectifier. Eight 22-μF capacitors (Samsung CL05A226MQ5N6J8) were used to create a capacitor bank with a total capacitance of 176 μF. A Zener diode (5.6 V, 100 mW, Comchip CZRZ5V6B-HF) was used for overvoltage protection. A low-dropout regulator with fixed internal output (2.7 V, Fairchild FAN25800, long-range applications, 3.3 V; ON Semiconductor NCP163AFCT330T2G, transcranial applications) managed voltage to the implants. A small outline μC (ATTiny 84A 3 × 3 mm; Atmel) with wide operational voltage capabilities was used to control μ-ILED activation. The μC firmware was programmed to power the μ-ILED with energy stored in the capacitor bank by sinking the current through the μ-ILED at relevant time points. The blue μ-ILED (CREE TR2227) current was limited by a current-limiting resistor (150 Ω for low load applications, 1 Ω for high load applications) to control irradiance. The red μ-ILED (Epistar ES-AEHRAX10) current was limited by the copper trace of the device (1 Ω) to control irradiance for high load applications.

Experimental Animals/Surgical Procedure. All procedures were performed in accordance with protocols approved by the Institutional Animal Care and Use Committee at Northwestern University. The right M2 was targeted for stereotactic injection in C57BL/6 mice (P40 to 60, Jackson; JAX000664) under isoflurane anesthesia using the following coordinates relative to bregma: anterior–posterior = + 2.2 mm, medial–lateral = + 1.0 mm, dorsal–ventral = −1.0 mm. Viruses (AAV9-syn-ChrimsonR-tdT, Addgene no. 59171; AAV8-syn-EGFP, University of North Carolina vector core) were diluted to a titer of ~5×10^{12} vg/mL in phosphate-buffered saline (PBS) and injected using a glass pipette and a microinjector. Around 2 to 3 wk after virus transduction, the skull was thinned (optional) to create a smooth surface over the previous injection site and the LED was attached to the skull using glue (KG58548R). The body of the device, which was sterilized in alcohol prior to implantation, was then secured to the skull using dental cement or Kwik-sil (KWIK-SIL, World Precision Instruments, LLC). Skin was then sutured over the device. Animals recovered for 48 to 72 h before the behavior experiment.

Behavioral Experiments. Animals were placed in a 15 × 15-cm arena equipped with an antenna connected to a Neurolux system. After a 2-min-long acclimatization period, animals were recorded for 3 min with the antenna turned off and then another 3 min with the antenna powered on. The devices were configured to deliver 2-ms long pulses at 20 Hz. Videos were recorded using a Raspberry Pi camera with a resolution of 1,280 × 720 at 25 fps. The snout, ears, hind legs, and the base of tail of each mouse were labeled using Deeplabcut (49). For each video, one frame per second was automatically selected in a uniform manner to be manually labeled, generating the training and testing dataset for the Deeplabcut algorithm. The test error with a *p*-cutoff value of 0.6 was 4.85 pixels. To quantify the rotational behavior of mice, one automatically labeled frame was selected per 0.5 s. The "head" position was defined as the centroid of the coordinates of the snout and ears, while the "back" position was defined by the centroid of the coordinates of two legs and the base of the tail. The body vectors were created from "back" to "head" positions for all labeled frames. Two body vectors separated by 0.5 s were designated as v_1 (x_1,y_1) and v_2 (x_2,y_2), respectively, and the angle of mice rotated in this period was calculated as follows:

$$\text{angle} = \arctan2(x_1y_2 - y_1x_2, x_1x_2 + y_1y_2).$$

The angle was converted from radian to degree (°). The cumulative degrees rotated during the initial 40 s were plotted for each experiment.

Immunohistochemistry. Immunostaining for c-Fos was performed on 60-μm vibratome sections by permeabilizing the tissue in 0.4% Triton-X in PBS for 15 min, blocking in PBS with 0.5% Triton and 10% bovine serum albumin for 1 h, performing the primary incubation in 1:5,000 rabbit anti–c-Fos (Synaptic Systems, category no. 226 003, RRID: AB_2231974) in PBS overnight at 4 °C, washing three times in PBS, performing the secondary incubation in 1:500 AlexaFluor647-conjugated donkey anti-rabbit (Thermo Fisher Scientific, category no. A-31573, RRID: AB_2536183), and washing three times in PBS as described in previous publications (50–53). After staining, the slices were mounted in a 9:1 mixture of glycerol and PBS containing Hoechst 33342 (2.5 μg/mL, Thermo Fisher Scientific). For c-Fos quantification, coronal brain sections were imaged using an Olympus VS120 microscope. All imaging parameters were constant across all samples, and each channel was imaged sequentially with a 10× objective. Two regions of interest (ROIs) of M2 (648×648 μm^2) per animal, selected from two different coronal sections, were used for analysis. Analysis was carried out in FIJI (54) using auto thresholding and particle analysis scripts. The same analysis parameters were applied across all ROIs.

Device Characterization. The power consumption of the device was characterized by measuring the current into the μC and μ-ILED with a current probe (Current Ranger LowPowerLab) at the defined system voltage. The voltage of the capacitor bank was measured with an oscilloscope (Siglent SDS1202X-E). A Siglent SSA3032X Spectrum Analyzer was used to verify the resonant frequency of the secondary antenna at 13.56 MHz. The power harvesting of devices with six, eight, and 10 antenna turns were characterized in the 70 × 70-cm cage by placing each device on a 3-cm mount at the center of the field and measuring the voltage output using a digital multimeter (DMM) (AN8008) with increasing loads added across the device. Arena power

mapping was performed by placing 10 turn devices at relative heights of 3, 6, and 8 cm from the cage floor and measuring voltage output with a DMM at a load of 10 kΩ throughout the arena with a 10-cm distance between each measurement point.

Wireless Programming. Implants were programmed using the setup shown in *SI Appendix*, Fig. S8, consisting of a laptop computer with a software interface to select stimulation parameters and power amplifier settings. External hardware included an RF amplifier (Neurolux, Inc.), tuner hardware (Neurolux, Inc.) and a custom TTL controller based on an Arduino Nano microcontroller (code available on GitHub) (image of setup shown in *SI Appendix*, Fig. S8*A*). Wireless power to the implant was modulated with a custom ON/OFF keying protocol sequence that was demodulated at the implant (*SI Appendix*, Figs. S7 and S8). The protocol utilized 12 bits of data to select up to 64 duty cycles and 64 frequencies, resulting in a programming time of 20 s. Correct programming was experimentally validated by μ-ILED output measurements using a custom photodetector and transimpedance amplifier setup.

Electromagnetic Simulation. The commercial software Analysis Systems 3D High Frequency Simulation Software (Ansys HFSS) was used to perform electromagnetic finite element analysis to determine the magnetic field distribution inside a 70 × 70 × 15-cm cage (length × width × height) enclosed by a copper wire antenna (diameter = 3 mm) with two loops. The bottom and top loops were placed at 4 and 11 cm, respectively, above the cage floor to create a uniform magnetic field. A lumped port was used to obtain the port impedance Z of the wire antenna and tune it to a working frequency of 13.56 MHz. An adaptive mesh (tetrahedron elements) and a spherical radiation boundary (radius of 5,000 mm) was adopted to ensure computational accuracy. The bulk conductivity, relative permittivity, and relative permeability of copper were $\sigma = 5.8 \times 10^7$ S/m, $\varepsilon = 1$, and $\mu = 0.99$, respectively.

Optical Characterization. Optical characterization was performed using an integrating sphere (OceanOptics FOIS-1) with a factory-calibrated light source (OceanOptics HL-3 plus). The μ-ILEDs were sourced with a current source (Keitheley 2231A-30–3, Tektronix) to provide a precise current to the device. The μ-ILEDs were mounted on a heat sink substrate to dissipate the excessive heat that could damage the μ-ILEDs. After light source calibration, the total irradiance flux spectra was collected using OceanView software, which contains the spectral power density (W/nm) of the light emitted by the μ-ILEDs. A spectra collection was repeated for each test driving current. The total power was then calculated by integration of the irradiance flux using a customized MATLAB script using an integration windows of 400 to 600 nm for blue μ-ILED and 550 to 700 nm for red μ-ILED.

Optical Simulations. The optical simulation of transcranial optogenetic stimulation was implemented using the Monte Carlo method (55). The volume of the numerical simulations was composed of $(850)^3$ bins, each with $(8\ \mu m)^3$, which represents a total volume of $(6.8\ mm)^3$ (56). The blue (460 nm) illumination source was a rectangular emitting surface of $0.22 \times 0.27\ mm^2$, whereas the red (628 nm) illumination source is $0.24 \times 0.24\ mm^2$, both with a 120° emission angle. In the simulation, 6.1×10^6 photons were launched. The material's optical properties (absorption, scattering coefficients, and dissymmetry factor: μ_a, μ_s, and g) for the simulations were brain tissue (both gray and white matter), skull (50 μm), skin (700 μm), and air, whose optical parameters (56–59) are summarized in *SI Appendix*, Table S2 for both wavelengths. An iterative comparison of optical parameters for brain tissue with measured experimental data revealed that optical parameters values stay within the margin of those reported in the literature (blue: $\mu_a = 1.5\ cm^{-1}$, $\mu_s = 300\ cm^{-1}$, and g = 0.83; red: $\mu_a = 0.6\ cm^{-1}$, $\mu_s = 75\ cm^{-1}$, and g = 0.83) and were used in the data analysis. Once the simulation for each wavelength was performed, postprocessing of the photon flux provided the illumination profiles, illumination volume, and irradiance decay normal to the μ-ILED's plane. The dimensional rendering for transcranial illumination with red light producing 5 mW of optical power was generated using Paraview 5.7.0 (60).

Characterization of Transcranial Light Propagation. The transcranial light propagation characterization in fresh mouse brain tissue was carried out using a homemade optical characterization apparatus (Fig. 4*G*). This system was comprised of a 10-mm-long 0.22 numerical aperture optical fiber cannula (0.2-mm core diameter) coupled to a high-sensitivity photomultiplier (Model 2151, New Focus, Inc.) using a fiber patch cable, both mounted on a one-dimensional linear translation stage (KMTS25E, Thorlabs, Inc.). A customized MATLAB script was implemented to synchronize the current source to drive the μ-LEDs (Keitheley 2231A-30–3, Tektronix), the data acquisition system (U3-HV, LabJack Corporation) to record the photovoltage generated by the photomultiplier, and the translation stage controller (KDC101, Thorlabs, Inc.). The red and blue μ-ILEDs were mounted side by side on a probe to allow simultaneous characterization, (Fig. 4*H*). At each 100-μm step, five test currents were probed simultaneously for blue illumination (1, 2, 3, 4, and 5 mA) and four for red illumination (1, 10, 20, and 30 mA). Preparations were set up within 1 h prior to the characterization, including an intact brain with a thinned skull at the location of the illumination site and a 1-mm hole on the opposite side for fiber insertion. Data were acquired as the cannula was inserted into the brain tissue to avoid artificial scattering by airgaps produced while retracting the fiber. The comparison of the simulation illumination power as a function of depth consisted in integrating an area equal to the core of the optical fiber (200 μm). Due to the distribution of the μ-ILEDs on the probe, the area of integration is not at the center of either μ-ILED, but in between.

Thermal Finite Element Analysis Model. Ansys 2019 R2 steady-state thermal and transient-state thermal were utilized for static-thermal and transient-thermal finite element modeling. The models were used to study the changes in temperature of the skull and brain tissue surrounding the μ-ILED. Components of the transcranial device, including the copper, polyimide (PI), and parylene encapsulation layers, were simulated in accurate layouts and with exact topologies within an octagonal area extending at least 0.95 mm in each direction from the μ-ILED. Program-controlled mechanical elements were used to simulate each model. The resolution of the mesh elements was set to four, and a minimum edge length of 6.5305 μm was used. Mesh convergence was ensured by using at least two elements in each direction. The thermal conductivity, heat capacity, and mass density of the materials used in the simulations was $130\ W \cdot m^{-1} \cdot K^{-1}$, $490\ J \cdot kg^{-1} \cdot K^{-1}$, and $8{,}920\ kg \cdot m^{-3}$ for the μ-ILED; $0.57\ W \cdot m^{-1} \cdot K^{-1}$, $4{,}068\ J \cdot kg^{-1} \cdot K^{-1}$, and $1{,}017\ kg \cdot m^{-3}$ for the CSF; $400\ W \cdot m^{-1} \cdot K^{-1}$, $385\ J \cdot kg^{-1} \cdot K^{-1}$, and $8{,}933\ kg \cdot m^{-3}$ for the copper traces; $0.37\ W \cdot m^{-1} \cdot K^{-1}$, $3{,}391\ J \cdot kg^{-1} \cdot K^{-1}$, and $1{,}109\ kg \cdot m^{-3}$ for the tissue; $0.126\ W \cdot m^{-1} \cdot K^{-1}$, $837\ J \cdot kg^{-1} \cdot K^{-1}$, and $1{,}110\ kg \cdot m^{-3}$ for the parylene encapsulation; and $0.12\ W \cdot m^{-1} \cdot K^{-1}$, $1{,}090\ J \cdot kg^{-1} \cdot K^{-1}$, and $1{,}420\ kg \cdot m^{-3}$ for the PI.

Characterization of Transcranial Thermal Propagation. The transcranial thermal impact characterization in mouse brain tissue ex vivo was carried out using a custom-built temperature probe and positioning stage. A source meter unit was used to measure signals from an 0201 negative-temperature coefficient sensor mounted on a 8.3-mm-long, 0.5-mm-wide, and 0.1-mm-thick custom probe to acquire the tissue temperature with millikelvin resolution (*SI Appendix*, Fig. S13). After calibration of the temperature sensor, the transcranial stimulation device was attached to the skull with surgical glue, analogous to the procedure described in *Experimental Animals/Surgical Procedure*. A one-dimensional positioning stage was used to insert the temperature sensor probe through a 1-mm opening opposite of the illumination site. Temperature measurements were taken at 0.5-mm increments starting from the skull at the illumination site. For each measurement, the device was operated at 10 Hz and 1% duty cycle for 5 min. Afterward, the temperature of the tissue was reset to ambient temperature by a cooldown period of 2 h.

Mechanical Simulations. An Ansys 2019 R2 Static Structural was utilized for static-structural finite element analysis simulations to study the elastic strain in the transcranial device and long-range device when the tethers were stretched. The components of the devices, including the copper traces, PI, μ-ILED, and parylene encapsulation layers, were simulated in accurate layouts and using their exact topologies. The model was simulated using program-controlled nonlinear mechanical elements with an element size manually input as 2E-2 mm. The Young's modulus (E) and Poisson's ratio (ν) are $E_{PI} = 4$ GPa, $\nu_{PI} = 0.34$; $E_{CU} = 121$ GPa, $\nu_{CU} = 0.34$; $E_{Parylene} = 2.7579$ GPa; $\nu_{Parylene} = 0.4$; and $E_{\mu\text{-ILED}} = 343$ GPa, $\nu_{\mu\text{-ILED}} = 0.28$. For each device, a fixed support was added to the respective face marked B in *SI Appendix*, Figs. S2 and S10. The applied strains for the transcranial device and long-range device serpentines were applied using a displacement as the load on the faces respectively marked A in *SI Appendix*, Figs. S2 and S10, and in the direction of the arrow shown in Figs. 2*E* and 4*E*, and were 75% (0.65 mm) for the transcranial device and 110% (~5.53 mm) for the long-range device.

Micro-CT/MRI Imaging. Mice were placed in an induction chamber and anesthetized with 3% isoflurane in oxygen. Mice were then transferred to an imaging bed with isoflurane delivered via nosecone (1 to 2%). A separate mouse bed was used for both imaging systems. After being placed in the prone position, the head of the mouse was immobilized with ear and tooth

bars. Respiratory signals were continuously monitored during μCT imaging with a digital system (Mediso). A preclinical microPET/CT imaging system (Mediso nanoScan scanner) was used to acquire images of the mice. Data were acquired with 2.17 magnification, 33 μm focal spot, 1 × 1 binning, using 720 projections over a full circle, an exposure time of 300 ms, and a peak tube voltage of 70 kV. A butterworth filter backprojection software (Mediso) was used to reconstruct each projection with a voxel size of 34 μm. A 9.4 T Bruker Bio spec MRI system with a 30-cm bore and a 12-cm gradient insert (Bruker Biospin, Inc.) was used to take MRI images. An MRI-compatible system (SA Instruments) was used to continuously monitor respiratory signals, and warm circuiting pads were used to maintain the body temperature of the animals. The animal bed was placed inside a 72-mm quadrature volume coil in transmit-only mode (Bruker Biospin, Inc.). The actively decoupled four-channel receiver coil (Bruker Biospin, Inc.) was mounted to the animal bed. Accelerated spin echo sequences (Turbo Rapid Acquisition with Relaxation Enhancement, TurboRARE) were used to collect images that were oriented in the axial, sagittal, and coronal configurations. The following specifications were used for each MRI scan: repetition time/echo time = 1,250 ms/21.3 ms, acquisition matrix = 256 × 256, field of view 3 × 3 cm, RARE factor 8, 7 to 13 slices of 0.75 to 1 mm thick, flip back enabled, 3 signal averages, and a total acquisition time of ∼2 min per scan. Data were visualized and reconstructed with Amira 6.7 (FEI) so that both MRI and μCT images could be manually superimposed over one another. Image artifacts in the CT images were further processed and reduced using Amira with nonlocal means filtering.

Data Availability. All data needed to evaluate the conclusions in the paper are present in the paper and/or supporting information. Additional data are available in the GitHub repository (https://github.com/jausra-arizona/GutrufLabDataCommunication.git). Code data have been deposited in Gutruf Lab Data Communication in Zenodo (DOI: 10.5281/zenodo.4947893) (61).

ACKNOWLEDGMENTS. We acknowledge the work and help of Anlil Brikha and Emily Waters of the Center for Advanced Molecular Imaging who performed the CT and MRI imaging. P.G. acknowledges Biomedical Engineering Department startup funds. J.A. acknowledges the support of National Heart, Lung, and Blood Institute NIH Grant No. 5T32HL007955-19. Y.K. acknowledges the support of National Institute of Neurological Disorders and Stroke Grant R01NS107539, National Institute of Mental Health Grant No. R01MH117111, the Searle Scholar Award, the Beckman Young Investigator Award, and the Rita Allen Foundation Scholar Award. M.W. was supported as an affiliate fellow of the NIH T32 AG20506.

1. P. Gutruf *et al*., Fully implantable optoelectronic systems for battery-free, multimodal operation in neuroscience research. *Nat. Electron.* **1**, 652–660 (2018).
2. P. Gutruf *et al*., Wireless, battery-free, fully implantable multimodal and multisite pacemakers for applications in small animal models. *Nat. Commun.* **10**, 5742 (2019).
3. G. Shin *et al*., Flexible near-field wireless optoelectronics as subdermal implants for broad applications in optogenetics. *Neuron* **93**, 509–521.e3 (2017).
4. V. K. Samineni *et al*., Fully implantable, battery-free wireless optoelectronic devices for spinal optogenetics. *Pain* **158**, 2108–2116 (2017).
5. K. L. Montgomery *et al*., Wirelessly powered, fully internal optogenetics for brain, spinal and peripheral circuits in mice. *Nat. Methods* **12**, 969–974 (2015).
6. A. Burton *et al*., Wireless, battery-free subdermally implantable photometry systems for chronic recording of neural dynamics. *Proc. Natl. Acad. Sci. U.S.A.* **117**, 2835–2845 (2020).
7. H. Zhang *et al*., Wireless, battery-free optoelectronic systems as subdermal implants for local tissue oximetry. *Sci. Adv.* **5**, eaaw0873 (2019).
8. J. Ausra *et al*., Wireless battery free fully implantable multimodal recording and neuromodulation tools for songbirds. *Nat. Commun.* **12**, 1968 (2021).
9. P. Gutruf, C. H. Good, J. A. Rogers, Perspective: Implantable optical systems for neuroscience research in behaving animal models—Current approaches and future directions. *APL Photonics* **3**, 120901 (2018).
10. S. I. Park *et al*., Stretchable multichannel antennas in soft wireless optoelectronic implants for optogenetics. *Proc. Natl. Acad. Sci. U.S.A.* **113**, E8169–E8177 (2016).
11. X.-T. Cao, W.-Y. Chung, An enhanced multiplication of RF energy harvesting efficiency using relay resonator for food monitoring. *Sensors (Basel)* **19**, 1963 (2019).
12. Y. Kozorovitskiy, R. Peixoto, W. Wang, A. Saunders, B. L. Sabatini, Neuromodulation of excitatory synaptogenesis in striatal development. *eLife* **4**, e10111 (2015).
13. C. K. Hu, H. E. Hoekstra, Peromyscus burrowing: A model system for behavioral evolution. *Semin. Cell Dev. Biol.* **61**, 107–114 (2017).
14. C. B. Alme *et al*., Place cells in the hippocampus: Eleven maps for eleven rooms. *Proc. Natl. Acad. Sci. U.S.A.* **111**, 18428–18435 (2014).
15. D. C. Rowland, Y. Roudi, M.-B. Moser, E. I. Moser, Ten years of grid cells. *Annu. Rev. Neurosci.* **39**, 19–40 (2016).
16. C. Ash, M. Dubec, K. Donne, T. Bashford, Effect of wavelength and beam width on penetration in light-tissue interaction using computational methods. *Lasers Med. Sci.* **32**, 1909–1918 (2017).
17. N. C. Klapoetke *et al*., Independent optical excitation of distinct neural populations. *Nat. Methods* **11**, 338–346 (2014).
18. J. Y. Lin, P. M. Knutsen, A. Muller, D. Kleinfeld, R. Y. Tsien, ReaChR: A red-shifted variant of channelrhodopsin enables deep transcranial optogenetic excitation. *Nat. Neurosci.* **16**, 1499–1508 (2013).
19. O. Yizhar *et al*., Neocortical excitation/inhibition balance in information processing and social dysfunction. *Nature* **477**, 171–178 (2011).
20. B. Y. Chow *et al*., High-performance genetically targetable optical neural silencing by light-driven proton pumps. *Nature* **463**, 98–102 (2010).
21. F. Zhang *et al*., Multimodal fast optical interrogation of neural circuitry. *Nature* **446**, 633–639 (2007).
22. R. Chen *et al*., Deep brain optogenetics without intracranial surgery. *Nat. Biotechnol.* **39**, 161–164 (2021).
23. S. M. Wellman, L. Li, Y. Yaxiaer, I. McNamara, T. D. Y. Kozai, Revealing spatial and temporal patterns of cell death, glial proliferation, and blood-brain barrier dysfunction around implanted intracortical neural interfaces. *Front. Neurosci.* **13**, 493 (2019).
24. T. Sasaki *et al*., Application of an optogenetic byway for perturbing neuronal activity via glial photostimulation. *Proc. Natl. Acad. Sci. U.S.A.* **109**, 20720–20725 (2012).
25. K. Beppu *et al*., Optogenetic countering of glial acidosis suppresses glial glutamate release and ischemic brain damage. *Neuron* **81**, 314–320 (2014).
26. Z. Xie, Q. Yang, D. Song, Z. Quan, H. Qing, Optogenetic manipulation of astrocytes from synapses to neuronal networks: A potential therapeutic strategy for neurodegenerative diseases. *Glia* **68**, 215–226 (2020).
27. Y. Jia *et al*., A mm-sized free-floating wirelessly powered implantable optical stimulation device. *IEEE Trans. Biomed. Circuits Syst.* **13**, 608–618 (2019).
28. K. Y. Kwon, H.-M. Lee, M. Ghovanloo, A. Weber, W. Li, Design, fabrication, and packaging of an integrated, wirelessly-powered optrode array for optogenetics application. *Front. Syst. Neurosci.* **9**, 69 (2015).
29. H. Lee, K. Y. Kwon, W. Li, M. Ghovanloo, A power-efficient switched-capacitor stimulating system for electrical/optical deep brain stimulation. *IEEE J. Solid-State Circuits* **50**, 360–374 (2015).
30. E. S. Boyden, F. Zhang, E. Bamberg, G. Nagel, K. Deisseroth, Millisecond-timescale, genetically targeted optical control of neural activity. *Nat. Neurosci.* **8**, 1263–1268 (2005).
31. S. Senova *et al*., Experimental assessment of the safety and potential efficacy of high irradiance photostimulation of brain tissues. *Sci. Rep.* **7**, 43997 (2017).
32. M. Keimasi, M. H. Azarian, M. G. Pecht, Flex cracking of multilayer ceramic capacitors assembled with Pb-free and tin–lead solders. *IEEE Trans. Device Mater. Reliab.* **8**, 182–192 (2008).
33. A. M. Lozano *et al*., Deep brain stimulation: Current challenges and future directions. *Nat. Rev. Neurol.* **15**, 148–160 (2019).
34. Y. Zhang *et al*., Battery-free, fully implantable optofluidic cuff system for wireless optogenetic and pharmacological neuromodulation of peripheral nerves. *Sci. Adv.* **5**, eaaw5296 (2019).
35. G. Nagel *et al*., Channelrhodopsin-2, a directly light-gated cation-selective membrane channel. *Proc. Natl. Acad. Sci. U.S.A.* **100**, 13940–13945 (2003).
36. L. Lu *et al*., Wireless optoelectronic photometers for monitoring neuronal dynamics in the deep brain. *Proc. Natl. Acad. Sci. U.S.A.* **115**, E1374–E1383 (2018).
37. T. Mager *et al*., High frequency neural spiking and auditory signaling by ultrafast red-shifted optogenetics. *Nat. Commun.* **9**, 1750 (2018).
38. H. M. Peixoto, R. M. S. Cruz, T. C. Moulin, R. N. Leão, Modeling the effect of temperature on membrane response of light stimulation in optogenetically-targeted neurons. *Front. Comput. Neurosci.* **14**, 5 (2020).
39. L. A. V. Magno *et al*., Optogenetic stimulation of the M2 cortex reverts motor dysfunction in a mouse model of Parkinson's disease. *J. Neurosci.* **39**, 3234–3248 (2019).
40. C. N. Bedbrook *et al*., Machine learning-guided channelrhodopsin engineering enables minimally invasive optogenetics. *Nat. Methods* **16**, 1176–1184 (2019).
41. N. Ulanovsky, C. F. Moss, Hippocampal cellular and network activity in freely moving echolocating bats. *Nat. Neurosci.* **10**, 224–233 (2007).
42. M. J. Wohlgemuth, C. Yu, C. F. Moss, 3D hippocampal place field dynamics in free-flying echolocating bats. *Front. Cell. Neurosci.* **12**, 270 (2018).
43. W. Zhao, F. Garcia-Oscos, D. Dinh, T. F. Roberts, Inception of memories that guide vocal learning in the songbird. *Science* **366**, 83–89 (2019).
44. Y. El-Shamayleh, G. D. Horwitz, Primate optogenetics: Progress and prognosis. *Proc. Natl. Acad. Sci. U.S.A.* **116**, 26195–26203 (2019).
45. Y. El-Shamayleh, A. M. Ni, G. D. Horwitz, Strategies for targeting primate neural circuits with viral vectors. *J. Neurophysiol.* **116**, 122–134 (2016).
46. H. Benveniste, N. H. Diemer, Cellular reactions to implantation of a microdialysis tube in the rat hippocampus. *Acta Neuropathol.* **74**, 234–238 (1987).
47. Y. Xie *et al*., In vivo monitoring of glial scar proliferation on chronically implanted neural electrodes by fiber optical coherence tomography. *Front. Neuroeng.* **7**, 34 (2014).
48. E. R. Hascup *et al*., Histological studies of the effects of chronic implantation of ceramic-based microelectrode arrays and microdialysis probes in rat prefrontal cortex. *Brain Res.* **1291**, 12–20 (2009).
49. A. Mathis *et al*., DeepLabCut: Markerless pose estimation of user-defined body parts with deep learning. *Nat. Neurosci.* **21**, 1281–1289 (2018).

50. M. Wu *et al*., Attenuated dopamine signaling after aversive learning is restored by ketamine to rescue escape actions. *eLife* **10**, e64041 (2021).
51. M. Wu, S. Minkowicz, V. Dumrongprechachan, P. Hamilton, Y. Kozorovitskiy, Ketamine rapidly enhances glutamate-evoked dendritic spinogenesis in medial prefrontal cortex through dopaminergic mechanisms. *Biol. Psychiatry* **89**, 1096–1105 (2021).
52. L. Xiao, M. F. Priest, J. Nasenbeny, T. Lu, Y. Kozorovitskiy, Biased oxytocinergic modulation of midbrain dopamine systems. *Neuron* **95**, 368–384.e5 (2017).
53. L. Xiao, M. F. Priest, Y. Kozorovitskiy, Oxytocin functions as a spatiotemporal filter for excitatory synaptic inputs to VTA dopamine neurons. *eLife* **7**, e33892 (2018).
54. J. Schindelin *et al*., Fiji: An open-source platform for biological-image analysis. *Nat. Methods* **9**, 676–682 (2012).
55. L. Wang, S. L. Jacques, L. Zheng, MCML—Monte Carlo modeling of light transport in multi-layered tissues. *Comput. Methods Programs Biomed.* **47**, 131–146 (1995).
56. A. N. Yaroslavsky *et al*., Optical properties of selected native and coagulated human brain tissues in vitro in the visible and near infrared spectral range. *Phys. Med. Biol.* **47**, 2059–2073 (2002).
57. H. Soleimanzad, H. Gurden, F. Pain, Errata: Optical properties of mice skull bone in the 455- to 705-nm range. *J. Biomed. Opt.* **22**, 49802 (2017).
58. C. P. Sabino *et al*., The optical properties of mouse skin in the visible and near infrared spectral regions. *J. Photochem. Photobiol. B* **160**, 72–78 (2016).
59. S. L. Jacques, Optical properties of biological tissues: A review. *Phys. Med. Biol.* **58**, R37–R61 (2013).
60. J. Ahrens, B. Geveci, C. Law, "ParaView: An end-user tool for large data visualization" in *Visualization Handbook*, C. D. Hansen, C. R. Johnson, Eds. (Butterworth-Heinemann, 2005), pp. 717–731.
61. J. Ausra, jausra-arizona/GutrufLabDataCommunication: Data Communication Code (Version v1.0.0). *Zenodo*. http://doi.org/10.5281/zenodo.4947893. Deposited 14 June 2021.